On the manufacturing of low temperature activated $Sr_{0.9}La_{0.1}TiO_{3-\delta}$-$Ce_{1-x}Gd_xO_{2-\delta}$ anodes for solid oxide fuel cell

Angela Gondolini* (1), Elisa Mercadelli (1), Guillaume Constantin (2,3), Laurent Dessemond (2,3), Vitaliy Yurkiv (4,5), Rémi Costa (4) and Alessandra Sanson (1)

(1) Institute of Science and Technology for Ceramics (ISTEC) of the National Research Council (CNR), Via Granarolo 64, I-48018 Faenza (RA), Italy

(2) Université Grenoble Alpes, Laboratoire d'Electrochimie et de Physico-Chimie des Matériaux et des Interfaces, F-38000 Grenoble, France

(3) CNRS, Laboratoire d'Electrochimie et de Physico-Chimie des Matériaux et des Interfaces, F-38000 Grenoble, France

(4) German Aerospace Centre (DLR), Institute of Technical Thermodynamics, Pfaffenwaldring 38-40, 70569 Stuttgart, Germany

(5) University of Illinois at Chicago (UIC), Department of Mechanical and Industrial Engineering, 842 W. Taylor St., 60607 Chicago, USA

* Corresponding author: Tel.: +39 0546 699732; fax: +39 0546 46381.

E-mail address: angela.gondolini@istec.cnr.it (A. Gondolini).

Abstract

Lanthanum doped strontium titanate – gadolinium doped cerium oxide (LST-GDC) anodic layers are sintered in air and further reduced *in-situ* at low temperature (750°C) avoiding usually performed pre-reduction treatment at high temperature. The influence of various milling techniques and of powders with different specific surface area, on the microstructures of screen-printed anodes, is investigated. The combination of milling and sonication processes is efficient in reducing aggregation of the anode powders. The anode performance is improved when a planetary milling step is involved in the preparation of the screen printing inks. The

use of gadolinium doped cerium oxide with high specific surface area decreases the polarization resistance. The rate of hydrogen oxidation is also enhanced by increasing porosity.

Keywords: LST-GDC anode, perovskite ceramic, ceramic process, screen printing, SOFC anode preparation

1. Introduction

Solid oxide fuel cells (SOFCs) are one of the most promising energy conversion devices due to their high efficiency, modularity, low emissions and the possibility to be directly fueled with natural gas, liquefied petroleum gas (LPG) and alcohols [1,2]. Presently, one of the major shortcomings about the utilization of these hydrocarbon fuels in SOFCs is associated with the anode compartment. Even though the commonly used Ni-based cermet shows high catalytic activity for hydrogen oxidation and electronic conductivity, it still faces high level of sintering (due to the coarsening in operando), high sensitivity towards carbon deposition and sulfur poisoning [3,4]. In addition, the poor redox stability of the Ni-based cermet still remains one of the major drawbacks. Therefore, intensive efforts have been devoted to replace the traditional Ni-cermet materials. Perovskite oxides, in particular $SrTiO_3$ –based compounds have attracted particular attention over the past years due to their decent conductivity, good dimensional stability and higher tolerance and resistance towards sulfur poisoning and carbon depositions [5-8]. Tuning the substitution and stoichiometry levels on A- and B-sites of $SrTiO_3$ – based compounds (La, Nb, Y and Ce) allows to achieve good catalytic activity for hydrogen oxidation, electrical conductivity and chemical stability in respect to the other perovskite-based materials at 700-850°C [7, 9]. For instance, the electrical conductivity of Y-$SrTiO_3$ (YST) materials changes on the basis of the concentration of strontium in their structure. With the strontium concentration from 87 to 91 atom%, the YST presented metallic-type

behavior (conductivity around 100 S cm^{-1} at 800°C), however increasing the Sr-amount between 95 and 99atom% the conductivity decreased down to 0.01 S·cm^{-1} at 800°C.

Among the different Ln-doped strontium titanates compositions, La-doped $SrTiO_3$ (LST) has shown good chemical and dimensional stability in wide ranges of temperature and oxygen partial pressure [6]. In addition LST composite shows good stability against sulfur poisoning and carbon deposition [13-15]. In particular $Sr_{0.9}La_{0.1}TiO_3$ composition has demonstrated an acceptable electrical conductivity level under SOFC anode condition and the air sintered – $Sr_{0.9}La_{0.1}TiO_3$ has negligible linear expansion in cyclic redox tests [13,14].

However, this material shows lower electrochemical performance than Ni-based anode under humidified hydrogen. For this reason, LST is combined with other oxide ion conductors to improve its electrochemical performances [16]. In this context, Gd -doped CeO_2 (GDC) is generally considered [17-18] instead of the conventionally used yttria-stabilized zirconia (YSZ) thanks to its significantly higher performance in both humidified H_2 and CH_4 [10, 11] and to its much better resistance to sulfur poisoning [12].

High temperatures and reducing atmospheres are required to produce highly conductive anode materials based on modified $SrTiO_3$, either during the material preparation or prior to testing [6]. The general approach used to process $SrTiO_3$-based materials implies sintering at high temperatures (>1300°C) under reducing conditions or sintering in air and a subsequent reduction treatment at temperature higher than 800°C [6]. Some authors [19-23] reported that *in-situ* reduction is a desirable processing step in order to eliminate a potentially expensive preparation step. A brief overview of LST performances, reduced in different conditions, is reported in Table 1.

Table 1. Brief overview of the testing condition, conductivity, power density of different type of LST-based pellet and cells reduced in different conditions.

Sample	Reduction	Testing condition	Conductivity	Fuel Cell configuration	Pre-reduction	Testing condition	Power Density	Ref.
LST_A- dense pellet (density~92%)	Reduction *in situ* at 900°C for more than 20 h	T= 900°C	2.75 S cm^{-1}	Electrolyte supported Cell	650°C in 5% H_2-Ar and 600°C for >12h *in situ*	3% humidified H_2 and O_2 at 600°C	0.146 W cm^{-2}	[20]
LST_A- dense pellet (density~92%)	Pre-reduction at 1050°C for 6h in 5% H_2-Ar	T= 900°C	25 S cm^{-1}	Electrode supported Cell	Pre-reduced LST 1100°C	3% humidified H_2 and O_2 at at 750°C	0.54 W cm^{-2}	[20]
LST, LSTNb Dense (density~80-90%) and porous (density~70%) pellets	Reduction *in situ* for at least 24 h in 5% H_2-Ar	T=930°C	Up to 7 S cm^{-1}	-	-	-	-	[21]
Porous samples (57-68 % of relative density)	Pre-reduction 1100-1300°C for 10h in 5% H_2-Ar	T=880°C	Up to 44 S cm^{-1}	-	-	-	-	[22]
LST_A- dense pellet (density 88%)	Pre-reduction 1050°C for 72h in 5% H_2-Ar	T=880°C	38 S cm^{-1}	-	-	-	-	[23]
LST_A- dense pellet (density 88%)	Reduction *in situ* upon 24h in 5% H_2-Ar	T=880°C	1.30 S cm^{-1}	-	-	-	-	[23]

Savaniu and Irvine [20] reported conductivities values of about 3 $S \cdot cm^{-1}$ (at 750°C) for dense $La_{0.2}Sr_{0.7}TiO_3$ pellet sintered in air at 1450°C for 12 hours. Pre-reduction at 1050°C for 6 hours in 5% H_2-Ar yielded conductivity of 25 $S \cdot cm^{-1}$ at the same testing temperature. Slater et al. [21] reported conductivity of dense reduced *in-situ* $La_{0.6}Sr_{0.1}TiO_3$ of 7 $S \cdot cm^{-1}$ at 930°C, in agreement with literature data for dense and porous bars [23]. The performances of $La_{0.4}Sr_{0.6}TiO_3$ anodes reduced in the experimental setup at 1000°C in 4% hydrogen-argon were fairly good (at 0.7 V, 340 $mA \cdot cm^{-2}$) but degraded rapidly over the testing period. Despite the remarkable increase of studies dedicated to LST-based anodes [24-28], this reduction at temperature above 1000°C is challenging in practical environment. Indeed this thermal treatment in reducing environment is not compatible with the sintering of the cathode material which would have to occur in air and thus necessarily re-oxidize the LST. This high temperature activation would thus imply to be made during an additional step during the manufacturing, with two separated atmospheres for the anode and the cathode which would necessarily imply higher costs. A cost effective and easy route could be to consider this reduction step during the sealing of the stack when the separation of the atmospheres between the anode and

the cathode is effectively made. When considering glass-ceramic material as the most promising sealant suitable for dual atmosphere operation [29], this restricts nonetheless the temperature to ca. 850°C at the maximum [30], which is lower than the minimal temperature to achieve the high conductivity of LST reported previously. Moreover, fuel cells anodes are subject to redox cycles during on/off cycles which will in turn impact negatively the level of conductivity of the LST by reoxidizing Ti^{3+} into Ti^{4+}. Even if the LST have been previously reduced at higher temperature, this original level of conductivity, governed by the ratio Ti^{3+}/Ti^{4+}, will not be recovered at the operating temperature due to the slower kinetic of equilibration, resulting in performance decrease. As a consequence, this challenges the redox cyclability of this electrode material.

In this study, the upper temperature is set to 800°C due to the thermo-mechanical limit of the thin film electrolyte of the Metal Supported Cell, for which this anode is intended for. For those reasons, we investigated and developed LST based anode activated at low temperature (i.e. below 800°C), which is compatible with the manufacturing route of full cells, the stacking, and the operation.$La_{0.1}Sr_{0.9}TiO_{3-\delta}$ –GDC anodic layers were produced in air, similarly to the mainstream manufacturing route of Solid Oxide Cells by using the conventional screen printing technique and directly reduced in the experimental setup at 750°C avoiding any pre-reduction treatment at high temperature. In this work, the aim is to identify a route for developing screen printed LST based anode layers sintered in air to be implemented in metal foam supported cell [31] and *in-situ* activated at 750°C by tuning the microstructure of the composite anode and the related manufacturing parameters. Therefore, the procedure of ink preparation and its effect onto the microstructure and electrochemical performance of the composite anode was evaluated on button symmetrical cells.

2. Experimental

Commercially available $La_{0.1}Sr_{0.9}TiO_{3-\delta}$ (LST, Cerpotech, Norway), $Gd_{0.1}Ce_{0.9}O_{2-\delta}$ (GDC10,

Treibacher, Austria), $Gd_{0.2}Ce_{0.8}O_{2-\delta}$ (GDC20M, Fuelcellmaterials, USA) with specific surface areas of 6.34, 9.10 and 36.5 m^2g^{-1}, respectively, were used as starting materials.

2.1 Fabrication processes

For the inks preparation, terpineol was considered as solvent, furoic acid as dispersant whereas ethyl cellulose (EC, Fluka, Italy) and carbon black (Thermax-Cancarb, USA) were added as binder and pore former respectively. The pore former was the 15 vol% with respect to the powder volume.

The starting LST-GDC powder was milled for 5 hours using conventional ball milling or planetary milling (Pulverisette, Fritsch, Germany) using zirconia grinding media and, respectively, polyethylene and zirconia jars. Dispersant and binder were separately dissolved in the total amount of terpineol necessary for the ink production. The dispersant, pore former and binder were added in a sequence to the milled suspension, and stirred for 5 minutes. The sonicating treatment was performed after each addition using a sonicating probe (Sonicator, ultrasonic processor XL, USA) for 15 minutes with an output power of 80 Watt. The as-prepared ink was, then, milled in a three-roll mill equipped with zirconia rollers of nanometric finishing (Exakt 80E, Germany).

The prepared ink was screen printed with a semi-automatic screen printer (AUR'EL 900, AUREL Automation s.p.a., Italy) onto both sides of YSZ sintered pellet (diameter = 18.5 mm, thickness = 2 mm). The final diameter of the screen printed electrodes was 16 mm. The number of passes for each ink composition was optimized in order to obtain a sintered thickness of the final electrode layer of 15 µm. After the screen printing process, the layers were dried in IR furnace (Ero Electronic SrL, Italy) in static air at 80°C for 15 minutes and sintered at 1100°C for 5 hours.

2.2 Characterization methods

The particle size distributions of the LST-GDC powders were determined using a dynamic

light scattering analyzer (DLS Nano S, Malvern UK). The starting powders morphology was investigated by scanning electron microscopy (Field Emission Gun - Scanning Electron Microscopy, FEG-SEM, ΣIGMA, Zeiss, Germany). The thermogravimetric (TG) and differential scanning calorimetry (DSC) analyses of the inks were carried out at a heating rate of 10°C min^{-1} in a simultaneous thermal analyzer (STA 449, Netzsch, Selb/Bavaria).

Structural, microstructural and morphological characterization of the cross-sections and of the surface of the symmetrical cells was performed thorough FEG-SEM. Samples cross-sections were prepared by vacuum embedding of the cell in epoxidic resin, followed by a mirror polishing.

For the porosity determination of the sintered anodes, the SEM micrographs of the polished fracture surfaces were binarized and analyzed using the ImageJ software.

The structure of the anode was characterized by X-ray diffraction (D8 ADVANCE, LynkEye detector- Bruker AXS, Germany) using CuKα radiation in the 10–80◦2Θ range, scan rate of 0.02°, and 185 s equivalent per step.

Electrochemical performance of symmetrical cells was evaluated by means of polarization curves and impedance spectroscopy measurements. The schematic illustration of experimental apparatus is given in Fig. 1.

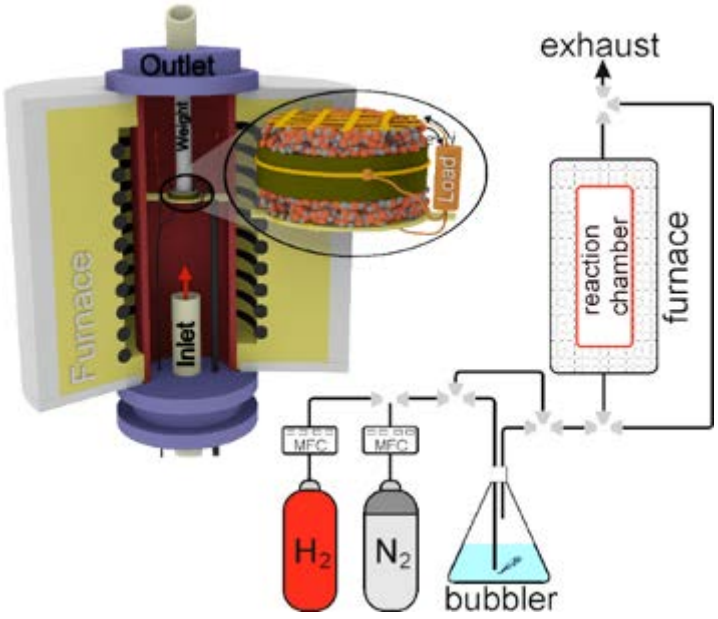

Fig. 1. Illustration of the electrochemical experimental apparatus.

The process-flow diagram (Fig. 1) of the experimental set-up illustrates inlet gasses, water bubbler and reactive chamber. All electrochemical measurements have been performed with high flow rate of 50 mL·min^{-1}·cm^{-2} using carefully controlled gas mixture of H_2+3%H_2O, thus, maintaining nearly uniform composition of the gasses along the investigated cell. Humidified hydrogen was supplied to the reactive chamber by bubbling hydrogen gasses through a room temperature water bath. Fine gold grids (680 mesh·cm^{-2}) used as current collector were placed on both sides of the cells prior to the electrochemical testing. Measurements were performed in a three-electrode configuration using a gold ring around the YSZ pellet as the reference electrode. Gold was chosen to avoid any catalytic contribution to the oxidation of hydrogen [32]. A mechanical pressure was applied on the grids to improve the electrical contacts. The completed button cells have active diameter of app. 16 mm, which leads to an active area of app. 2 cm^2. Prior to the electrochemical measurements, during the start-up heating, the cell was exposed to a stream of dilute reducing gas (N_2) until reaching 800 °C. When the target temperature was achieved, the inlet fuel was switched to H_2/H_2O mixture, and after reaching a stable open circuit potential (OCP), an automated load was used to measure polari-

zation curves and impedance spectra. The more detailed description of experimental apparatus as well as methodology of measurements is given elsewhere [33]. The reduction period at 800 °C was fixed equal to 2 hours. Indeed, screening measurements were performed as a function of the reduction period for times up to 12 hours. A monotonic decrease of the electrode resistance was recorded during 2 hours indicating the reduction of the anode material. No further decrease was evidenced for longer times.

The electrochemical experiments were performed in a furnace that maintains a required uniform temperature range of 650 – 850 °C. Impedance spectra were recorded for all temperatures with the voltage stimulus of 20 mV between $5 \cdot 10^{-3}$ Hz and $2 \cdot 10^{4}$ Hz. Polarization curves were recorded in a potentiostatic mode within the same temperature range and reported in terms of current density as a function of the electrode overvoltage.

3. Results and discussion

3.1 Characterization of the starting powders

3.1.1 As-received and milled LST-GDC10

Prior to the preparation of the anodes the scanning electron microscopy (SEM) images were recorded of the starting LST ,GDC10 and GDC 20M powders (Figure 2 a), b) and c), respectively).

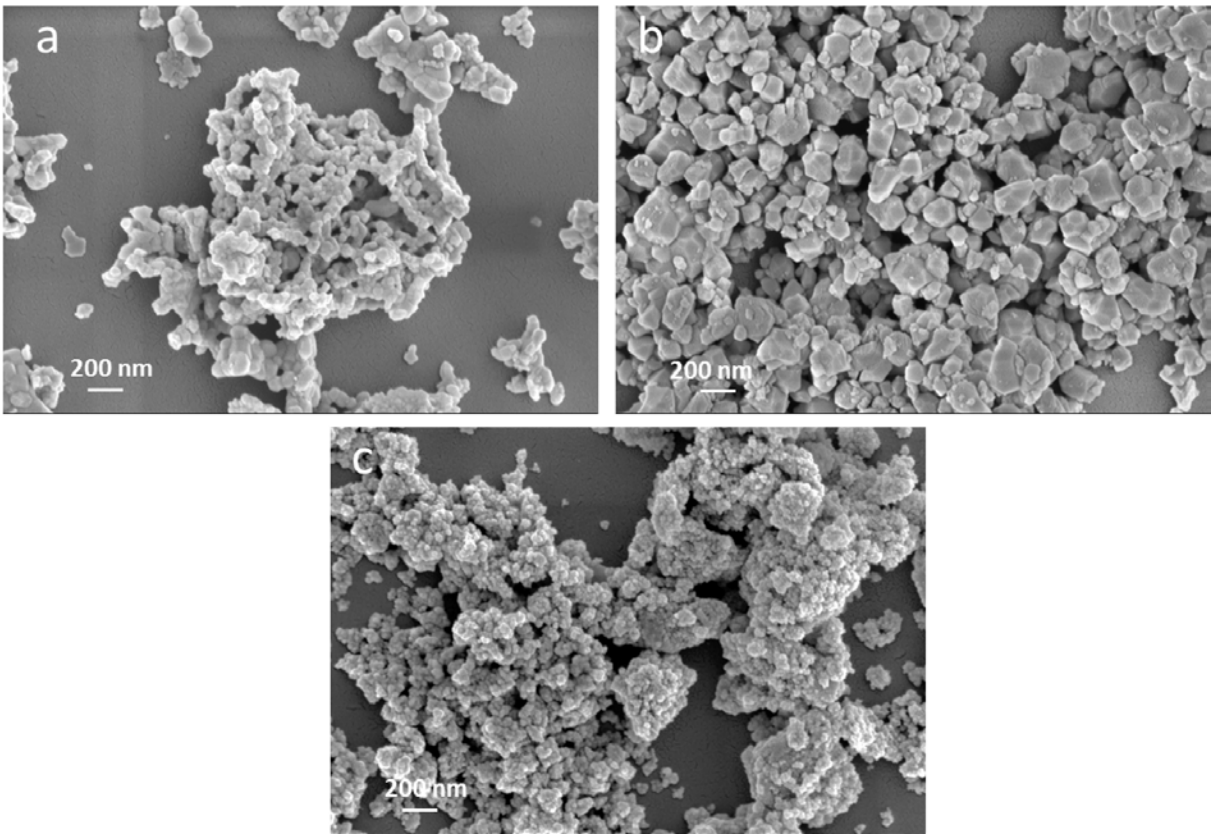

Fig. 2. SEM micrographs of the LST (a), GDC10 (b) and GDC20M (c) powders.

As can be seen in Fig. 2 the starting powders are formed by agglomerates of micrometric dimensions, which consist of nanometric round-shape particles.

The particle size distribution of the LST and GDC10 mixture (Figure 3 a) shows a bimodal distribution confirming the presence of large aggregates of micrometric dimension (3-8 μm).

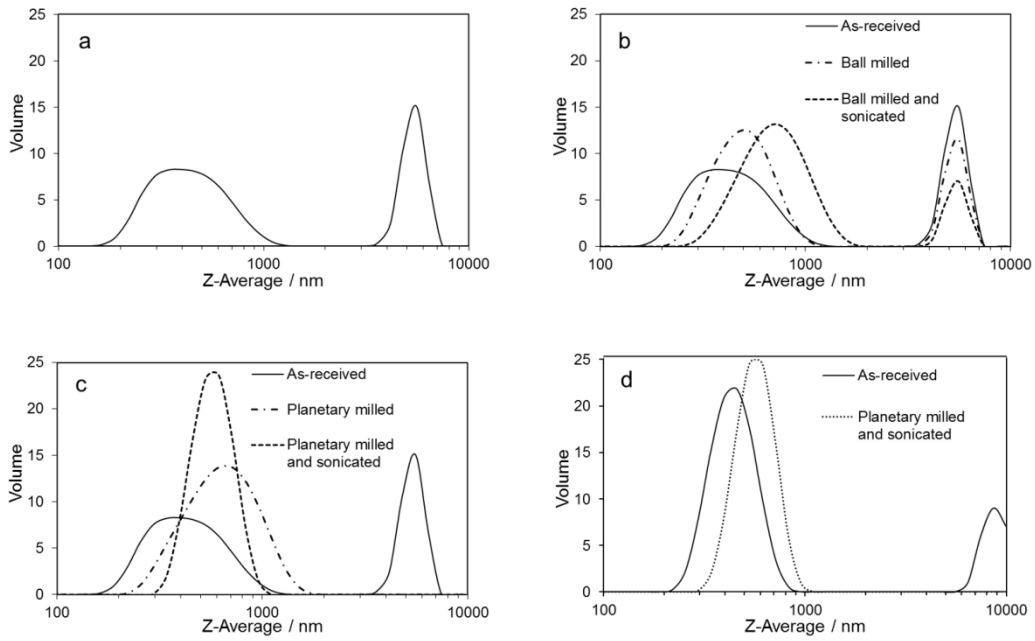

Fig. 3. Mean particle size (Z-Average) distribution of the mixture of LST and GDC10 (a). Mean particle size (Z-Average) distributions of the LST-GDC10 mixture treated with conventional ball milling and conventional ball milling plus sonication (b), of the LST-GDC10 mixture treated with planetary milling and planetary milling plus sonication (c) and of LST-GDC20M mixture treated with planetary milling plus sonication (d) compared to the ones of the as-received powder.

It is well known [34-35] that these aggregates can lead to a bad dispersion of the electron conducting phases affecting negatively the catalytic activity of the anode and must, therefore, be reduced.

As reported in the prior literature [36-39], the catalytic activity of the anodic layer is strongly linked to its microstructure and phases dispersion. These characteristics are generally related to the properties of the starting powders such as particle size distribution, specific surface area and mean particles diameters. To obtain the best powder dispersion and homogeneous microstructure of the anodic layer, a milling treatment of the starting powders is a common practice to break down the large aggregates and to obtain a sharper distribution. For doing so in this

study, conventional ball and planetary milling processes eventually coupled with a sonicating treatment were considered for the powder suspension.

The distribution of the powders processed with conventional ball milling and ball milling plus sonicating treatment compared to the as-received one (Figure 3 a) is reported in Figure 3 (b). The ball milling process produces a narrower distribution of the first peak reducing at the same time the aggregates between 3 and 8 μm. Moreover, a shifting of the first peak towards higher size value is observed due to the milling of the larger aggregates. This trend becomes more pronounced when the sonicating treatment is coupled with the milling process (Figure 3 b).

This combination of processes is therefore efficient in reducing the amount of aggregates of the anodic powder but not sufficiently strong to completely break down the aggregates in the 3-8 μm range. A stronger milling (i.e. planetary milling) was then considered. This energetic process was able to produce a monomodal distribution (Figure 3 c) and when coupled with a sonicating treatment the distribution of particles dimension was very sharp and centered at 530 nm.

The values of Mean Particle Diameter (MPD) of the processed LST-GDC10 distributions are reported in Table 2.

Table 2. Particle size distribution of LST-GDC10 and LST-GDC20M mixtures treated with different ball milling treatment eventually treated with the sonicating process (MPD: Mean particles diameters).

	Treatment	MPD (1^{st} peak)	MPD (2^{nd} peak)
I	As-received	340	5560
II	Ball milling	450	5500
III	Ball milling + sonicating	715	4800
IV	Planetary milling	570	-
V	Planetary milling + sonicating	530	-
VI	As-received (LST - GDC20M)	450	8640
VII	Planetary milling + sonicating (LST - GDC20M)	570	-

Considering these data, it is clear that the conventional ball milling either alone or in combination with a sonication is not very effective in produce a well dispersed mono-modal distribution (Treatments II and III- Table 1). The MPD of the first peak increases as a consequence of the breaking of the larger aggregates as clearly indicated by Figure 3 b). On the other hand, the planetary milling (Treatments IV and V- Table 1) is able to completely eliminate the large aggregates (2^{nd} peak) and with the help of a sonication process to push the MPD down to 530 nm.

3.1.2 High SSA LST-GDC20M

To better understand the influence of the specific surface area (SSA) of the starting powder on the electrical properties of the anodic layer, another commercial GDC (with higher SSA) was considered and coupled with LST. In particular, the GDC phase confers the necessary ionic conductivity to the anode [1-3] and therefore, with the increasing of the specific surface area of this powder the oxygen supply of the anode should be improved. The GDC considered (20M, Fuelcell materials, USA) shows a specific surface area of 36.5 $m^2 \cdot g^{-1}$ with respect to the 9.10 $m^2\ g^{-1}$ of the powder previously considered (GDC10) and a Gd doping level slightly higher (20mol% compared to the 10mol%). The SEM micrograph of this powder (Figure 2 c) shows the lower particle size of the GDC20M with respect to the one shown by the GDC10 (Figure 2 b).

Depending on the elaboration route and the corresponding microstructure, the critical gadolinium concentration in doped ceria to achieve the highest ionic conductivity was determined to be approximately 20 mol% [2]. However, it was also reported that the ionic conductivity of $Ce_{0.9}Gd_{0.1}O_{2-\delta}$ was higher than that of $Ce_{0.8}Gd_{0.2}O_{2-\delta}$ at 500 °C [3]. By preparing the GDC solid solutions from high purity CeO_2 and Gd_2O_3 powders, it was shown that the total conductivity of $Ce_{1-x}Gd_xO_{2-\delta}$ maximize at the composition x=0.15. Moreover, the total conductivities of $Ce_{0.8}Gd_{0.2}O_{2-\delta}$ and $Ce_{0.9}Gd_{0.1}O_{2-\delta}$ were found rather close above 500 °C [4]. Considering the same microstructure of the investigated anodes and since the electronic conductivity of LST is higher than the ionic conductivity of GDC in reducing conditions, one can assume that the effective conductivity of LST-GDC anodes do not depend on the gadolinium content in the chosen experimental conditions. Accordingly, any variation of the resistances should be related to the microstructure parameters of the electrodes, as confirmed hereafter.

In order to compare the results obtained with the LST-GDC10 mixture, the LST-GDC20M was processed using planetary milling and sonicating treatments.

The particle size distributions and MPD of this powder are reported, respectively, in Figure 3

(d) and Table 1 (Treatments VI and VII). Also in this case, the particles size distribution becomes mono-modal after the milling and sonicating treatments showing a MPD equal to 570 nm. This result very similar to the one reported for the LST-GDC10 mixture, is attributed to the higher difficulty of de-agglomeration of the powder with the higher SSA (GDC20M).

3.2 Production and characterization of LST-GDC inks

The inks formulation produced with the processed LST-GDC10 and the LST-GDC20M are reported in Table 3.

Table 3. Screen printing inks formulations (vol%) for anode materials.

	Ink1 LST-GDC10	Ink2 LST-GDC10	Ink3 LST-GDC20M
LST	3.39	3.36	3.16
GDC	3.39	3.36	3.16
Solvent	82.61	81.79	77.03
Dispersant	2.14	3.11	8.74
Binder	5.57	5.51	5.19
Pore former	2.90	2.87	2.71

The ink containing the as-received LST-GDC10 (Ink1 LST-GDC10) was produced for comparison. Since the powder treatments lead to a de-agglomeration of large aggregates and, therefore, to an increasing of the free particles surface, the amounts of deflocculant to be added to the inks containing the processed LST-GDC10 and LST-GDC20M (respectively ink2

and ink3) were re-optimized. In particular, these amounts were determined through analyses of the particle size distribution of suspensions containing the processed LST-GDC10 and LST-GDC20M with different quantities of deflocculant. The suspensions presenting the lower MPD (corresponding to the ones containing the 39 and the 58 vol% of deflocculant for, respectively, LST-GDC10 and LST-GDC20M) are the ones better dispersed.

The TG and DSC analyses of the produced inks are reported in Figure 4 (a) and (b) respectively.

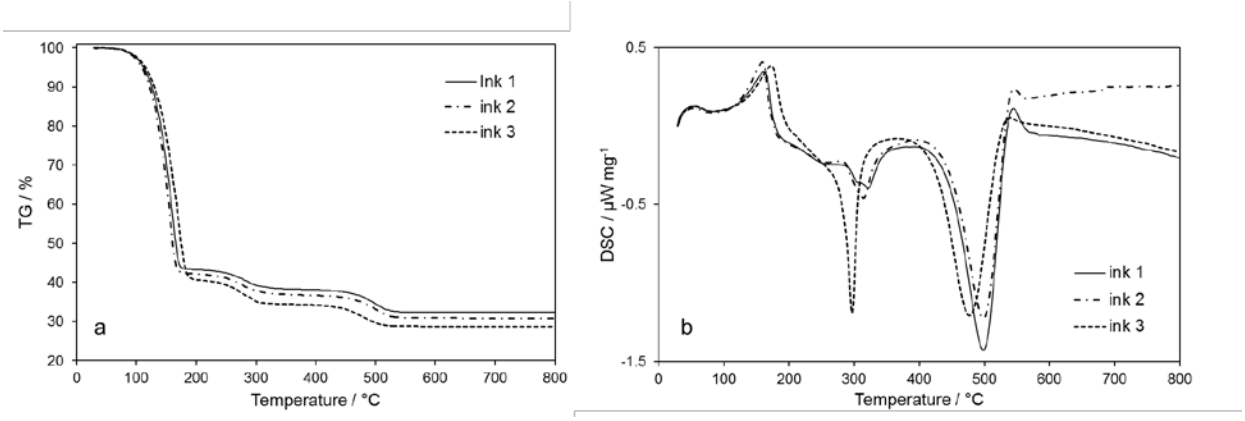

Fig. 4. TG (a) and DSC (b) analyses of the anodic inks.

The TG curves show that the elimination of all the organic components of the inks occurs through 3 steps. The first weight loss associated to an endothermic peak at 160°C is related to the evaporation of the solvent. The second weight loss at around 300°C is linked to the decomposition of the binder and deflocculant while the third one is finally due to the elimination of the pore former. The DSC curve of the ink3 presents a stronger exothermic 2nd peak (at about 300°C) due to the substantial higher amount of deflocculant added to this composition in respect to the ones of the other inks. The shift of the pore former decomposition peaks at slightly lower temperatures ($T_{ink1} > T_{ink2} > T_{ink3}$) is due to the increase of the specific surface area of the GDC, a well-known catalyst for the carbonaceous species decomposition [40].

The thermal cycle for the sintering of the anodic layer was optimized on the basis of these results using a slow heating rate (30°C·h^{-1} instead of 100°C·h^{-1}) between 150 and 600°C.

3.3 Characterization of symmetrical cells

3.3.1 Microstructural characterization

The anodic films were screen printed onto both sides of the YSZ pellets in order to obtain anodic films of about 15µm of thickness. After sintering at 1100°C for 5 hours, the deposited films perfectly adhere to the YSZ substrate without any sign of delamination (Figure 5).

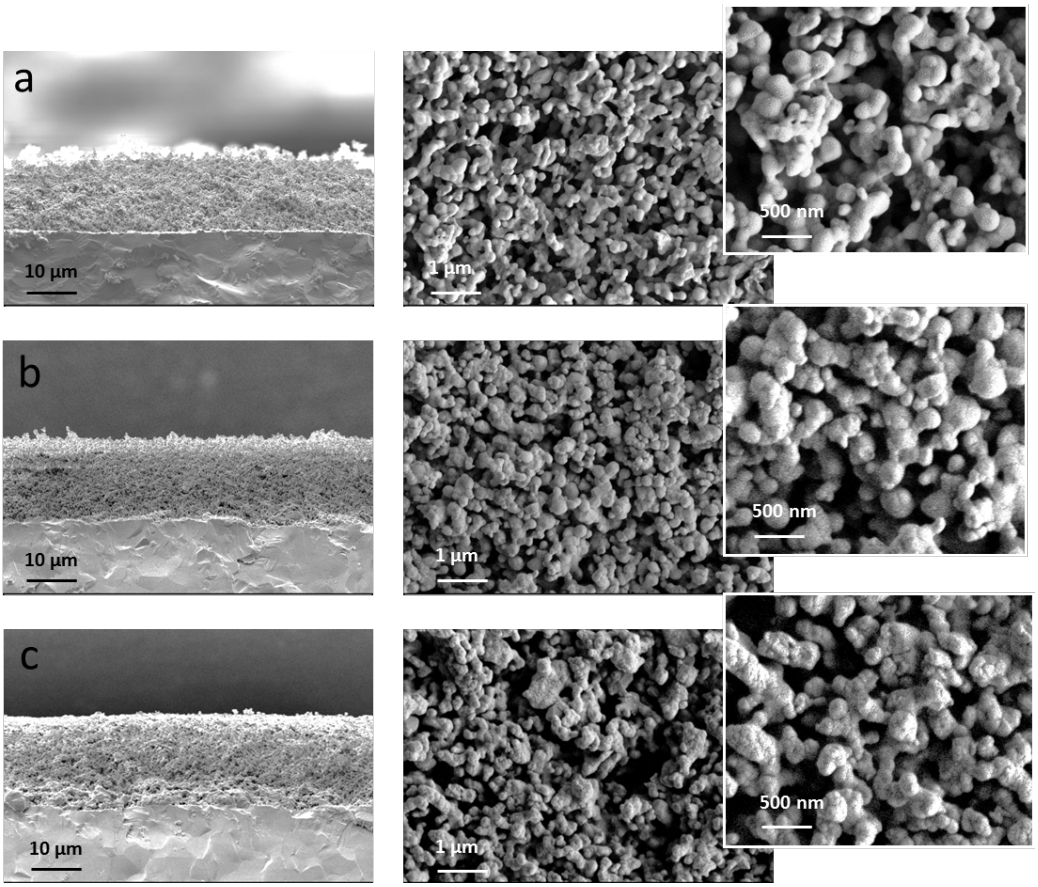

Fig. 5. SEM micrograph of the fresh fracture and of the surface of the anode produced with ink1 LST-GDC10 (a), ink2 LST-GDC10 (b) and ink3 LST-GDC20M (c).

The XRD analysis of the electronic layer shows the presence of the crystalline LST (JCPDS reference: PDF#55-926) and GDC10 (JCPDS reference: PDF#01-075-0161) phases. The microstructures produced with the three inks (Figure 5) are comparable. No significant changes (particles size, morphologies and distribution) can be observed in the final layer microstructures obtained using inks 1 and 2, the layer containing the GDC 20M (ink 3) shows the pres-

ence of smaller particles among the bigger LST ones.

All the anodes produced show deposited layer well-leveled also in the case of the ink that showed the highest viscosity (Ink3 LST-GDC20M). This is probably due to the softening action of the binder ascribed to the IR heating that is able to decrease the viscosity of the deposited ink during the drying process [41]. The IR drying produces, in fact, screen printed layers more smoothed in respect to the ones obtained with the conventional drying thanks to its heating propagation from the bulk to the superficial part of the film on the contrary of what happens for the conventional route.

All the produced anodes show very high values of porosity (Table 4). The trend of the porosity values is in agreement with the vol % of the organics present in the different anodic layers.

Table 4. Values of porosity and of the organics in the green layers of the as-produced anodic layer.

	Porosity (vol %)	Organics in the green layer (vol %)
Ink1	56± 1	58.4
Ink2	60 ± 3	63.1
Ink3	68 ± 2	72.4

3.3.2 Electrochemical characterization of the symmetrical cells

Electrochemical performance of the symmetrical cells was measured. Figure 6 shows polarization curves and impedance spectra of the LST-GDC20M cell for different temperatures in 97 % H_2+3% H_2O at OCP. By repeating impedance spectroscopy and potentiostatic measurements on two similar symmetrical cells (i.e. elaborated with the same ink), the inaccuracy

on series and polarization resistance is found lower than 9% in the chosen temperature range. Under load, the inaccuracy on the current density can reach 15% for electrode overpotentials higher than 0.5 V. It is lower than 10% in the vicinity of OCP.

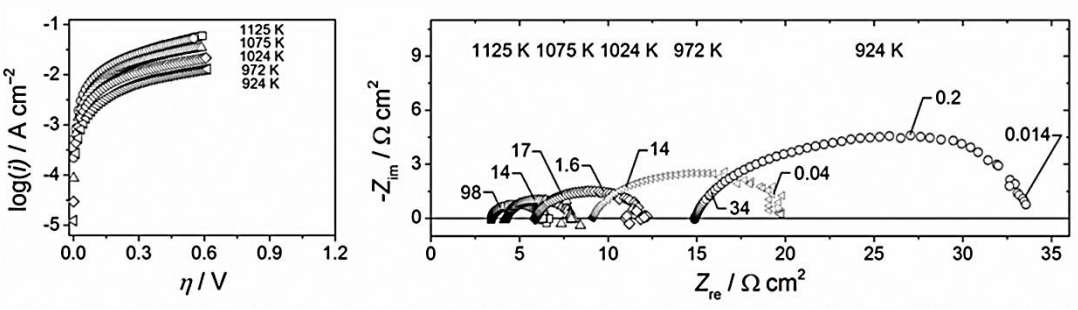

Fig. 6. Polarization curves and impedance spectra as measured for the cell LST-GDC20M over temperature range between 650 and 850 °C (924 K and 1125 K). Numbers in the Nyquist plot indicate frequencies in Hz.

The electrochemical responses of the different anodes at 750 °C are shown in Figure 7.

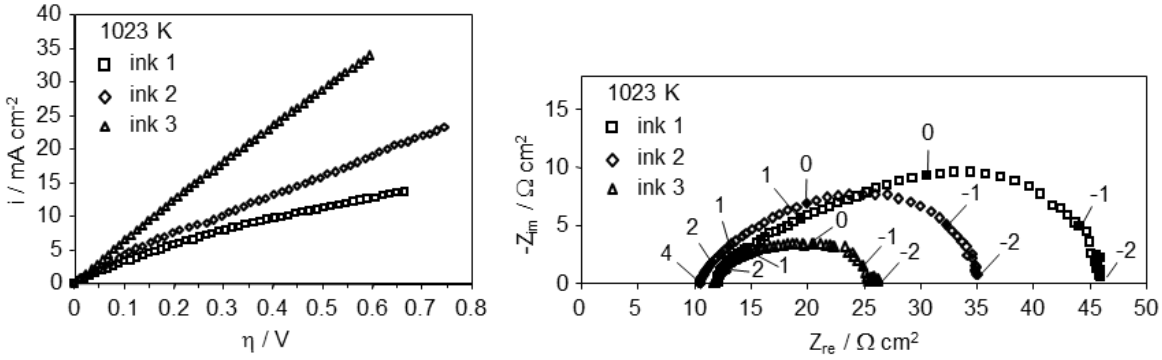

Fig. 7. Polarization curves and impedance spectra as measured for the different anodes at 750 °C (1023 K) in wet H_2. Numbers in the Nyquist plot indicate the logarithm of the frequencies in Hz.

At fixed temperature, the frequency distribution of the electrode characteristic remains nearly similar whatever the ink used for preparing the electrode. This indicates that the whole electrode reaction mechanism remains unchanged, regardless of the electrode microstructure. It is

worth noting that the R_s values are close for all the electrodes. By assuming that the position of the reference electrode around the YSZ pellet is nearly the same for all studied anodes, this result suggests that the contact area at the anode/YSZ interface do not significantly vary as a function of the ink. By using literature data on YSZ conductivity [42,43] and from the thickness of YSZ and electrode area, the calculated values of R_s are within 15% equal to the experimental values (e.g. 10.5-12.3 $\Omega.cm^2$ at 750 °C). This indicates that the resistance of YSZ mainly governs the magnitude of the series resistance. For a fixed electrode thickness (15 µm), this also suggests that the distribution on current lines within the electrode volume is roughly identical. Accordingly, the recorded variation of polarization resistance (Figure 7) is not related to any different active electrode volumes.

Figure 8 shows polarization curves recorded on symmetrical cells with LST-GDC10 and LST-GDC20M anodes produced from ink 1 and ink 3 respectively. Within the experimental accuracy, the similar current densities versus electrode overpotential confirm that any variation of the performance mainly originates from the electrode microstructure.

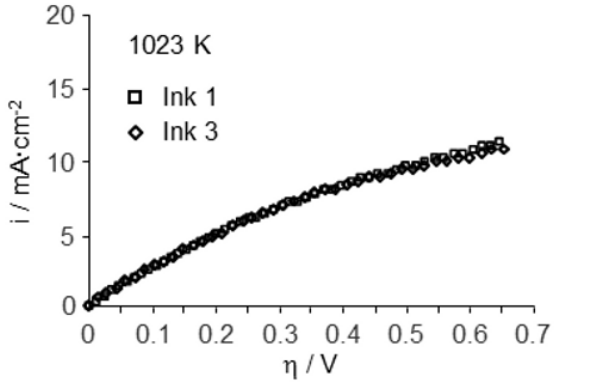

Fig. 8. Polarization curves for LST-GDC10 (ink1) and LST-GDC20 (ink 3) anodes at 750 °C (1023 K) in wet H_2.

At the equilibrium, the series and polarization resistances (R_s and R_{pol}) are decreasing functions of the measuring temperature (Figure 9). At this stage, it is worth mentioning that measurements were not performed during successive thermal cycles. No failure, which could be

related to different TEC values between LST and GDC, of the investigated assemblies was detected in the chosen experimental conditions.

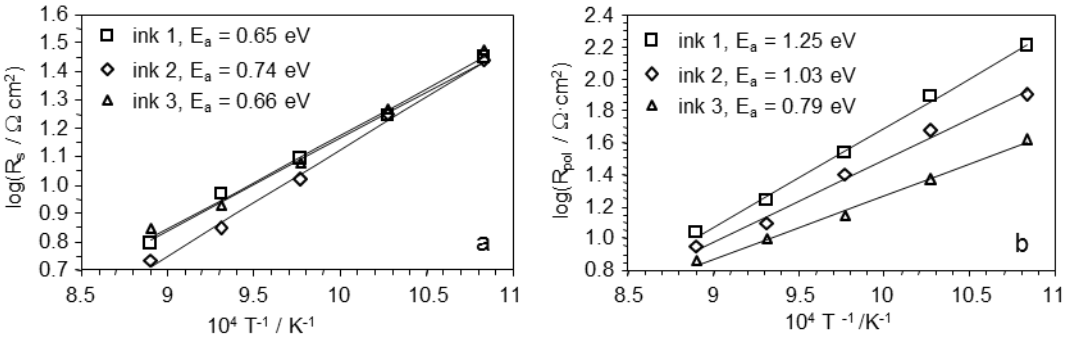

Fig. 9. Arrhenius diagrams of (a) series and (b) polarization resistances at OCP in wet H_2 for the different anodes.

The activation energies for both resistances have been calculated from the corresponding Arrhenius diagrams. The activation energy for R_s varies between 0.65 and 0.74 eV, which is in well agreement with values reported in the literature for YSZ above 650°C [44,45]. The highest R_{pol} values are obtained for the ink 1, and the lowest for the ink 3. The values of activation energy for R_{pol} agree with literature data on LST-based anodes [19,46]. The ink 2 and 3 present a monomodal particle size distribution centred at around 530-570 nm, whereas the ink 1 presents a bimodal particles distribution with mean diameters centred at 340 nm and 5560 nm. A fine and homogeneous particles size yields a higher gas exchange surface area. The anode layer made with the ink 3 shows a higher porosity of 68 % than 60 % and 56 % for the ink 2 and 1, respectively. A higher porosity allows a better gas phase distribution inside the electrode layer and thus yields lower polarization resistance (Figure 9).

A limitation of the reaction kinetics is evidenced for the sample made with inks 1 and 2 (Figure 7) and corresponds to an increasing magnitude of the low frequency part of the electrode characteristic with the anode potential below 800°C. At this stage, this limitation is likely to be related to gas transport if one refers to the frequency distribution of such a process [47-49].

So the rate of the hydrogen oxidation rate is enhanced by increasing the gas exchange surface area, e.g. decreasing the particles size, and by favoring the gas phase transport within the volume of the electrode, e.g. increasing the porosity, in agreement with a modeling approach [28].

4. Conclusions

In this study, $La_{0.1}Sr_{0.9}TiO_{3-\delta}$ based anodic layers were produced in air and directly reduced *in-situ* at 750°C avoiding any pre-reduction treatment at higher temperature. Different LST-GDC anodes were obtained by screen printing and tested to evaluate performance of symmetrical button cells. It was found that the symmetrical cell performance is improved when a planetary milling process coupled with a sonication treatment is employed during the screen printing inks preparation. In particular the use of GDC with high specific surface area leaded to decrease the polarization resistance. By increasing the specific area of GDC powders (a factor of 4), the anode resistance decreases by a factor of 2.5 at 750°C. Future works will be devoted to additionally improve the anodic layer performance by using LST powder with higher SSA and using infiltration treatment of LST and/or GDC in order to increase the gas exchange surface area of the electrode.

Acknowledgments

This work was funded by the European Union's Seventh Framework Program (FP7/2007-2013) for the Fuel Cells and Hydrogen Joint Technology Initiative under grant agreement n°303429.

The authors thank the Dr. A. Chesnaud and Dr. D. Masson (Centre des Matériaux, Mines-ParisTech) for providing the YSZ pellets.

References

[1] S.C. Singhal, K. Kendall, High temperature solid oxide fuel cells fundamentals. Design and application, first ed., Elsevier, Amsterdam, 2003.

[2] N.Q. Minh, Ceramic fuel cells, J. Am. Ceram. Soc. 76 [3] (1993) 563-588.

[3] O. Yamamoto, Solid oxide fuel cells: fundamental aspects and prospects, Electroch. Acta. 45 (2000) 2423-2435.

[4] M. Dokiya, SOFC system and technology, Solid State Ionics 152-153 (2002) 383-392.

[5] M. K. Rath, K.T. Lee, Properties and electrochemical performance of $Sr_{0.8}La_{0.2}TiO_{3-\delta}$-$Ce_{0.8}Gd_{0.2}O_{2-\delta}$ composite anodes for intermediate temperature solid oxide fuel cells. J. Alloys Compounds 657 (2016) 537-545.

[6] M. C. Verbraeken, T. Ramos, K. Agersted, Q. Ma, C. D. Savaniu, B. R. Sudiredy, J. T. S. Irvine, P. Holtappels, F. Tietz, Modified strontium titanates: from defect chemistry to SOFC anodes, RSC Adv. 5 (2015) 1168-1180.

[7] A. Atkinson, S. Barnett, R. J. Gorte, J. T. S. Irvine, A. J. McEvoy, M. Mogensen, S. C. Singhal, J. Vohs, Advanced anodes for high-temperature fuel cells, Nat. Mat. 3 (2004) 17-27.

[8] S. Tao, J.T.S. Irvine, A redox-stable efficient anode for solid-oxide fuel cells, Nat. Mater. 2 (2003) 320-323.

[9] P. Holtappels, J.T.S. Irvine, B. Iwanschitz, L. Theil Kuhn, L. Y. Lu, Q. Ma, J. Malzbender, A. Mai, T. Ramos, J. Rass-Hansen, B. R. Sudireddy, F. Tietz, V. Vasechko, S. Veltzé, M.C. Verbraeken, Full Ceramic Fuel Cells Based on Strontium Titanate Anodes, An Approach Towards More Robust SOFCs. ECS Trans. 57 (2013) [1] 1175-1184.

[10] K.B. Yoo, G.M. Choi, Co-doped $La_{0.2}Sr_{0.8}TiO_3$ as a possible anode for the $LaGaO_3$-based Solid Oxide Fuel Cell, ECS Trans. 25 (2009) 2259-.2266.

[11] N. Danilovic, A. Vincent, J.L. Luo, K.T. Chuang, R. Hui, A.R. Sanger, Correlation of Fuel Cell Anode Electrocatalytic and ex situ Catalytic Activity of Perovskites $La_{0.75}Sr_{0.25}Cr_{0.5}X_{0.5}O_{3-\delta}$ (X = Ti, Mn, Fe, Co) Chem. Mater. 22 (2010) 957-965.

[12] S. K. Schubert, M. Kusnezoff, A. Michaelis, S. I. Breikhin, Comparison of the performances of single cell solid oxide fuel cell stacks with Ni/8YSZ and Ni/10CGO anodes with H2S containing fuel, J. Power Sources 217 (2012) 364–372.

[13] O.A. Marina, N.L. Canfield, J.W. Stevenson, Thermal, electrical, and electrocatalytical properties of lanthanum-doped strontium titanate, Solid State Ion. 149 (2002) 21-28.

[14] Z. Wang, M. Mori, Sintering Characteristics and Electrical Conductivity of ($Sr_{1-x}La_x$)TiO_3 Synthesized by the Citric Acid Method, J. Fuel Cell Sci. Technol. 8 (2011) 051018-051022.

[15] J. E. Sunstrom, S. M. Kauzlarich , P. Klavins, Synthesis, structure, and properties of lanthanum strontium titanate ($La_{1-x}Sr_xTiO_3$), Chem. Mater. 4 [2] (1992) 346–353.

[16] X. Shen, K. Sasaki, Highly redox-resistant solid oxide fuel cell anode materials based on La-doped $SrTiO_3$ by catalyst impregnation strategy, J Power Sources 320 (2016) 180-187.

[17] F. Liquan, X.Yueping, L. Lianbao, et al. Performance of $Gd_{0.2}Ce_{0.8}O_{1.9}$ infiltrated $La_{0.2}Sr_{0.8}TiO_3$ nanofiber scaffolds as anodes for solid oxide fuel cells, J. Power Sources 265 (2014) 125-131.

[18] K. Genji, K. Myoujin, T. Kodera, T. Ogihara, Synthesis and electrical properties of La doped $SrTiO_3$ powders by ultrasonic spray pyrolysis, Key Eng. Mater. 582 (2013) 115-118.

[19] M.C. Verbraeken, B. Iwanschitz, A. Mai, J.T.S. Irvine, Evaluation of Ca Doped $La_{0.2}Sr_{0.7}TiO_3$ as an Alternative Material for Use in SOFC Anodes, J. Electrochem. Soc. 159 (2012) F757-F762.

[20] C.D. Savaniu, J.T.S. Irvine, Reduction studies and evaluation of surface modified A-site deficient La-doped $SrTiO_3$ as anode material for IT-SOFC, J. Mater. Chem. 19 (2009) 8119–8128.

[21] P.R. Slater, D.P. Fagg, J.T.S. Irvine, Synthesis and electrical characterization of doped perovskite titanates as potential anode materials for solid oxide fuel cells, J. Mater. Chem. 7 (1997) 2495-2498.

[22] D. Neagu, J.T.S. Irvine, Structure and properties of $La_{0.4}Sr_{0.4}TiO_3$ ceramics for use as anode materials in solid oxide fuel cells, Chem. Mater. 22 (2010) 5042−5053.

[23] A. Yaqub, C. Savaniu, N.K. Janjua, J.T.S. Irvine, Preparation via a solution method of $La_{0.2}Sr_{0.25}Ca_{0.45}TiO_3$ and its characterization for anode supported solid oxide fuel cells, J. Mater. Chem. A 1 (2013) 14189–14197.

[24] M.R. Afshar, N Yan, B. Zahiri, D. Mitlin, K.T. Chuang, J.L. Luo, Impregnation of $La_{0.4}Ce_{0.6}O_{1.8}$-$La_{0.4}Sr_{0.6}TiO_{3-\delta}$ as solid oxide fuel cell anode in H_2S-containing fuels, J. Pow. Sources 274 (2015) 211-218.

[25] A. Yaqub, N.K. Janjua, C. Savaniu, JTS Irvine, Synthesis and characterization of B-site doped $La_{0.20}Sr_{0.25}Ca_{0.45}TiO_3$ as SOFC anode materials, Int. J. Hydrogen Energy 40 [1] (2015) 760-766.

[26] E. Kazakevicius, G. Tsekouras, K.A. Michalow-Mauke, S. Kazlauskas, T. Graule, Electronic Conductivity Enhancement of (La,Sr)TiO_3 with Nb-Doping on B-Site, Fuel Cells 14 [6] (2014) 954-960.

[27] B.R. Sudireddy, K. Agersted, Sintering and Electrical Characterization of La and Nb Co-doped $SrTiO_3$ Electrode Materials for Solid Oxide Cell Applications, Fuel Cells 14 [6] (2014) 961-965.

[28] V. Yurkiv, G. Constantin, A. Hornes, A. Gondolini, E. Mercadelli, A. Sanson, L. Dessemond, R. Costa, Towards understanding surface chemistry and electrochemistry of $La_{0.1}Sr_{0.9}TiO_{3-\alpha}$ based solid oxide fuel cell anodes, J. Power Sources 287 (2015) 58-67.

[29] J. Schilm, A. Rost, A. Poenicke, M. Kusnezoff, A. Michaelis, Ceramic Integration Technologies for Solid Oxide Fuel Cells, Int. J. Appl. Ceram. Technol., 9 (2012), 688–699.

[30] A.G. Sabato, G. Cempura, D. Montinaro, A. Chrysanthou, M. Salvo, E. Bernardo, M. Secco, F. Smeacetto , J. of Power Sources 328 (2016) 262-270.

[31] F. Han, R. Semerad, G. Constantin, L. Dessemond, R. Costa, Beyond the 3rd generation of planar SOFC: development of metal foam supported cells with thin film electrolyte, ECS

Trans. 68 [1] (2015) 1889-1896.

[32] T.H. Shin, S. Ida, T. Ishihara, Doped CeO_2–$LaFeO_3$ Composite Oxide as an Active Anode for Direct Hydrocarbon-Type Solid Oxide Fuel Cells, J. Am. Chem. Soc., 2011, 133 (48), pp 19399–19407.

[33] G. Constantin, C. Rossignol, P. Briois, a. Billard, L. Dessemond, E. Djurado, Efficiency of a dense thin CGO buffer layer for solid oxide fuel cell operating at intermediate temperature, Solid State Ionics. 249-250 (2013) 98–104.

[34] S. Ozkar, Enhancement of catalytic activity by increasing surface area in heterogeneous catalysis, Appl. Surface Science 256 (2009) 1272–1277.

[35] A. Gondolini, E. Mercadelli, A. Sanson, S. Albonetti, L. Doubova, S. Boldrini, Effect of the microwave heating on the properties of gadolinium-doped cerium oxide prepared by polyol method, J. Europ. Ceram. Soc. 33 (2013) 67-77.

[36] C. Xia, M. Liu, Microstructures, conductivities, and electrochemical properties of $Ce_{0.9}Gd_{0.1}O_2$ and GDC–Ni anodes for low-temperature SOFCs, Solid State Ionics 152-153 (2002) 423-430.

[37] R. M.C. Clemmer, S. F. Corbin, The influence of pore and Ni morphology on the electrical conductivity of porous Ni/YSZ composite anodes for use in solid oxide fuel cell applications, Solid State Ionics 180 [9-10] (2009) 721-730.

[38] F. Tietz, F.J. Dias, D. Simwonis, D. Stoever, Evaluation of commercial nickel oxide powders for components in solid oxide fuel cells, J. Europ. Ceram. Soc. 20 (2000) 1023-1034.

[39] C.M. Grgicak, R.G. Green, J.B. Giorgi, Control of microstructure, sinterability and performance in Co-precipitated NiYSZ, CuYSZ and CoYSZ SOFC anodes, J. Mater. Chem. 16 (2006) 885-897.

[40] A. Gondolini, E. Mercadelli, S. Albonetti, A. Sanson, Role of Different Solvents on the Purification of As-Synthesized Nano-$Ce_{1-x}Gd_xO_{2-d}$ Powders, J. Nanoscie. Nanotech. 15[5]

(2015) 3636-3640.

[41] A. Gondolini, E. Mercadelli, A. Sangiorgi, A. Sanson, Integration of Ni-GDC layer on a NiCrAl metal foam for SOFC application, J. Europ. Ceram. Soc. 37 [3] (2017) 1023-1030.

[42] T.Y. Yeh, R.D. Lin, J.S. Cherng, Significantly enhanced ionic conductivity of yttria-stabilized zirconia polycrystalline nano-film by thermal annealing, Thin Solid Films 544 (2013) 148-151.

[43] R. Fernandez-Gonzalez, T. Molina, S. Savvin, R. Morano, A. Makradi, P. Nunez, Fabrication and electrical characterization of several YSZ tapes for SOFC applications, Ceram. Int. 40 (2014) 14253-14259.

[44] S. P. S. Badwal. Zirconia-based solid electrolytes: microstructure, stability and ionic conductivity, Solid State Ionics 52 (1992) 23-32.

[45] N. Mahato, A. Banerjee, A. Gupta, S. Omar, K. Balani, Progress in material selection for solid oxide fuel cell technology: A review, Progr. Mater. Sci. 72 (2015) 141-337.

[46] D.N. Miller, J.T.S. Irvine, B-site doping of lanthanum strontium titanate for solid oxide fuel cell anodes, J. Pow. Sources, 196 (2011), 7323-7327.

[47] Q.X. Fu, F. Tietz, D. Stöver, $La_{0.4}Sr_{0.6}Ti_{1-x}Mn_xO_{3-\delta}$ Perovskites as Anode Materials for Solid Oxide Fuel Cells, J. Electrochem. Soc. 153 (2006), D74-D83.

[48] S. Primdhal, M. Mogensen, Gas diffusion impedance in characterization of solid oxide fuel cell anode, J. Electrochem. Soc. 145 (1998), 2431-2438.

[49] W.G. Bessler, Gas Concentration Impedance of Solid Oxide Fuel Cell Anodes
I. Stagnation Point Flow Geometry, J. Electrochem. Soc. 153 (2006), A1492-A1504.